International Journal of Hydrogen Energy 119 (2025) 73–81

Contents lists available at ScienceDirect

International Journal of Hydrogen Energy

journal homepage: www.elsevier.com/locate/he

# Synergistic electroreduction of $CO_2$ to $C_1$-$C_3$ gas products in a pressure-tolerant MEA system

Siyu Zhong [a,*], Wenwu Yang [b], Sida Liu [c], Roland Dittmeyer [a]

[a] Institute for Micro Process Engineering (IMVT), Karlsruhe Institute of Technology (KIT), Hermann-von-Helmholtz-Platz 1, 76344, Eggenstein-Leopoldshafen, Germany
[b] Institute of Nanotechnology (INT), Hermann-von-Helmholtz-Platz 1, 76344, Eggenstein-Leopoldshafen, Germany
[c] Institute of Biological and Chemical Systems-Functional Molecular Systems (IBCS-FMS), Karlsruhe Institute of Technology (KIT), Hermann-von-Helmholtz-Platz 1, Eggenstein-Leopoldshafen, 76344, Germany

ARTICLE INFO

Handling Editor: Søren Juhl Andreasen

*Keywords:*
$CO_2$ reduction
High pressure
Operation engineering
Cell voltage
Zero-gap electrolyzer

ABSTRACT

Electrochemical reduction of carbon dioxide offers a sustainable route to reduce $CO_2$ to combat climate change and advance renewable energy use. However, challenges such as high energy demand and unsatisfactory selective production of higher hydrocarbons ($C_{2+}$) hinder its practical implementation. This work investigates the effects of operating conditions on the performance of $CO_2$ electroreduction, based on an optimized zero-gap electrolyzer design and a high-pressure reaction setup. The results show that moderate temperatures can increase energy efficiency and selectivity, with Faradaic efficiencies over 40 % for $C_1$–$C_3$ gas products. High-pressure environments exceeding 10 bar can improve the availability and mass transport of $CO_2$, and suitable proportions of syngas for subsequent reuse can be generated in this harsh environment. Tandem-layer catalysts can enhance CO generation, highlighting the need for precise control of catalyst interactions. In addition, lower neutral electrolyte concentrations favor the formation of $C_{2+}$ products but consume higher energy compared to alkaline environments. These findings provide insights and strategies for optimizing $CO_2$ electrolysis systems, aiding the development of efficient and scalable technologies for practical applications.

## 1. Introduction

The electrochemical reduction of carbon dioxide ($CO_2$RR) offers a promising pathway for converting greenhouse gases into valuable chemicals and holds significant potential for mitigating climate change and advancing sustainable energy conversion [1,2]. The practicality of $CO_2$RR applications relies on the development of advanced electrochemical systems capable of delivering high reaction rates and product selectivity, all based on cost-effective and high-performance catalysts [3,4]. Despite notable advancements in synthesizing specific products under controlled laboratory research conditions [5,6], the widespread implementation of $CO_2$RR still faces persistent challenges, such as high energy demand and low selectivity to the desired products.

Copper-based materials are recognized as among the most effective catalysts for producing higher hydrocarbons $C_{2+}$ due to their distinctive ability to stabilize reaction intermediates during $CO_2$ reduction [7–10]. However, the distribution of products and the reaction efficiency are not solely dictated by catalyst properties but are also influenced by numerous operational factors within the electrolyzer. Variables such as electrolyte composition, electrode potential, temperature, and pressure play crucial roles in steering reaction pathways and energy conversion to favor specific products [11–15]. Furthermore, the design and operating conditions of the electrolyzer, encompassing features like gas diffusion electrode design and fluid flow dynamics, significantly affect mass transport which in turn may influence both activity and selectivity [16–18]. A thorough understanding of the interplay between these parameters is vital for achieving optimal $CO_2$RR performance.

Electrolyzer designs based on membrane electrode assemblies (MEA) are considered particularly promising for the scale-up of $CO_2$RR applications due to the compact architecture and minimized interfacial resistance, enabling high current density [19,20]. Conducting $CO_2$RR experiments under elevated temperature and pressure offers additional advantages, such as accelerating reaction kinetics, enhancing mass transfer, and improving product selectivity [21,22]. However, these conditions bring about technical challenges, such as the need for robust sealing and reliable safety measures for high-pressure environments, as well as ensuring the stability of catalysts and electrolytes under extreme conditions [23]. As a result, the development of advanced

* Corresponding author.
*E-mail address:* siyu.zhong@kit.edu (S. Zhong).

https://doi.org/10.1016/j.ijhydene.2025.03.234
Received 7 January 2025; Received in revised form 11 March 2025; Accepted 15 March 2025
Available online 20 March 2025

electrocatalytic systems capable of efficient and stable operation in such demanding settings has become a central focus in $CO_2$RR research.

Addressing these challenges necessitates optimizing the electrocatalysis process and systematically evaluating the impact of various operational parameters. This means fine-tuning factors such as temperature, pressure, electrolyte properties, and catalyst architecture should be taken into consideration for a universal $CO_2$RR system. At this point, the test chain of the $CO_2$RR system based on a modified zero-gap electrolyzer and compatible with a variety of reaction conditions was built and introduced in this work. By analyzing the combined effects of these variables on product distribution, current efficiency, and energy consumption in the modified electrolysis reactor and system, this work aims to provide valuable insights into the development of efficient, stable, and scalable $CO_2$RR systems for future applications.

## 2. Experimental section

### 2.1. Preparation for MEA

Electrodes were prepared by spray-depositing catalyst ink onto a gas diffusion layer (GDL). For consistency, the active area of both cathode and anode electrodes was standardized to 12 $cm^2$. A regular copper cathode was prepared by manually spraying the ink, which had been made by ultrasonically dispersing 30 mg of copper nanopowder (APS 20–50 nm, 99.9 %, Thermo Scientific Chemicals) and 40 μL of 5 wt % Nafion solution in 2 mL of isopropanol for 20 min, onto a carbon paper substrate (Sigracet 39 BB) placed on a hotplate at 80 °C. This process produced a cathode catalyst layer with a mass loading of approximately 1.5 mg/$cm^2$. Additionally, the same mass of silver nanocatalyst (APS 20–40 nm, 99.9 %, Thermo Scientific Chemicals) was spray-coated onto a copper-coated electrode to form a CuAg@C cathode, or copper was deposited onto a pre-coated silver electrode to form an AgCu@C cathode. The total catalyst loading for both tandem catalyst layer configurations was approximately 2.8–3.0 mg/$cm^2$. The preparation of the anode catalyst layer followed a similar spraying process, in which 30 mg of iridium oxide nanopowder was deposited on a platinum-coated titanium fiber felt GDL to establish a uniform catalyst layer. The anion exchange membranes (Sustainion® X37-50 Grade RT) were activated in 1 M KOH for 24 h, followed by 0.1 M $KHCO_3$ for an additional 12 h. Then the membrane was sandwiched between the cathode and anode catalysts to form an MEA.

### 2.2. Characterizations

The surface characterization and energy-dispersive X-ray spectroscopy (EDS) element mapping of the samples were performed using a Zeiss Gemini SEM 500 microscope equipped with a thermal Schottky field emission cathode. Cross-sectional SEM images of the coated samples were obtained through a JEOL JXA 8530F microscope. Contact angle measurements were performed in a DSA25S Drop Shape Analyzer, with 5 μL deionized water droplets for imaging and angle determination.

### 2.3. High-pressure test bench modification

The MEA was placed between two custom-made titanium flow field plates, with titanium bolts on the sides acting as current collectors, as described in our previous work [24]. Then the assembly was enclosed by two stainless steel plates equipped with plug-in heating cartridges, which precisely control the temperature of the electrolyzer via the temperature indicator and controller (TIC). The process diagram of high-pressure electrochemical system is shown in Fig. 1. This system incorporated two high-pressure back-pressure valves (BPR) and an electronic pressure indicator and controller (PIC) to maintain equal pressure levels in the cathode and anode chambers of the MEA electrolyzer. Meanwhile, multiple pressure indicators and temperature indicators were built in to track dynamic changes within the system. Flow management was accomplished by a flow indicator and controller (FIC) and HPLC pumps, which delivered gases and anode liquid to the electrolyzer accurately and stably even at high pressures. For temperature-dependent electrocatalysis experiments, the stainless-steel cylinder containing 0.8 L of water and the glass bottle containing 3 L of anolyte were maintained at a temperature of 50 °C for any experiments above room temperature. The stainless-steel pipe at the cathode inlet was heated to the same experimental temperature of the electrolyzer.

### 2.4. Electrocatalytic performance

Electrochemical $CO_2$ reduction performance was studied using a Biologic VSP-300 potențiostat equipped with a 10-A current booster. In the zero-gap MEA electrolyzer setup, the cell voltage was measured as the potential difference between the cathode and anode, with no iR compensation applied. The anolyte was circulated through the system using an HPLC pump at a flow rate of 30 mL/min. The $CO_2$ flow rate to

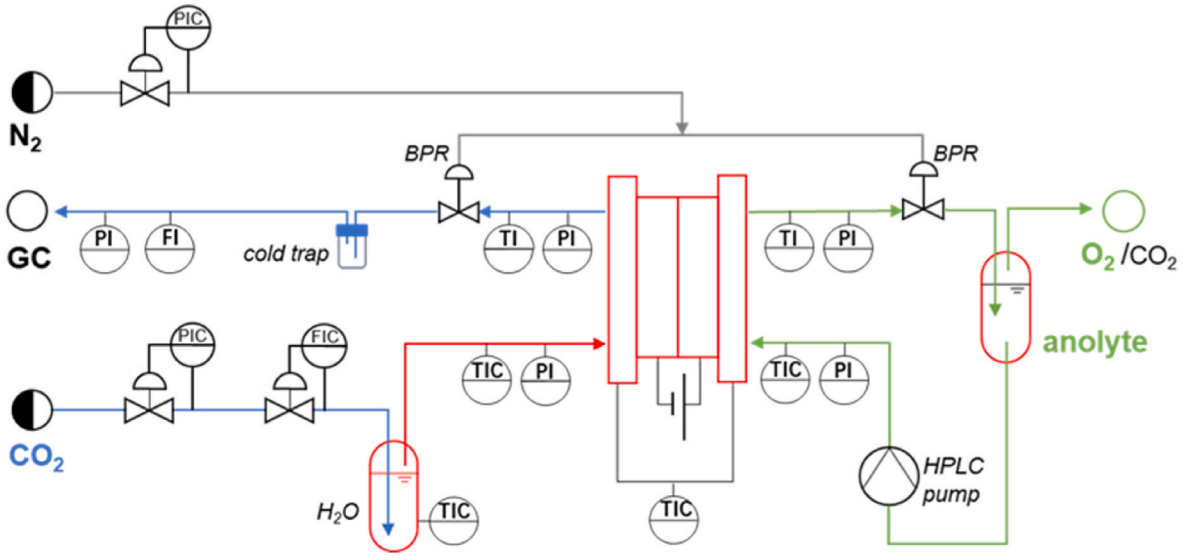


**Fig. 1.** Process diagram of high-pressure $CO_2$RR system. Blue is the cathode flow, green is the anode flow, and red is the heating element. (For interpretation of the references to colour in this figure legend, the reader is referred to the Web version of this article.)

the cathode was precisely regulated to 90 standard cubic centimeters per minute (sccm) using a mass flow controller (SLA5800 series, Brooks), where the $CO_2$ gas was preconditioned by bubbling through a cylinder filled with water. To get rid of residual air from the system, $CO_2$ was introduced 10 min before initiating each electrolysis experiment. Three consecutive linear sweep voltammetry (LSV) tests were performed at a scan rate of 30 mV/s to a potential of −3 V to reduce trace amounts of copper oxide and activate the electrodes, before each chronopotentiometry on a fresh cathode.

### 2.5. Product quantification

The gas product composition was analyzed in a gas chromatograph (SHIMADZU 2010 plus) equipped with an HP-PLOT Q column. Ultra-high purity argon gas (99.9999 %) was employed as the make-up gas. The chromatograph was fitted with a flame ionization detector (FID) to quantify $C_1$–$C_3$ hydrocarbons and a thermal conductivity detector (TCD) to hydrogen. Both detectors were calibrated by a series of commercial standard gases before analysis. A float-type flux indicator (FI) located before GC served as a reference to verify the gas flow rate. The system was programmed to automatically collect gas samples every 15 min, and data from at least three consecutive measurements were recorded to ensure accuracy in calculating the Faradaic efficiency and associated error bars at each current density. Although trace amounts of formic acid and ethanol were detected in the liquid collected at the cathode outlet, the distribution of gaseous products was regarded as the predominant outcome under the reaction conditions investigated in this study. The Faradaic efficiency (FE) of the gas products was determined using the following equation:

$$FE_{(x)} = \frac{Q_i}{Q_{total}} \times 100\,\% = \frac{n \times m \times v \times \frac{Fp}{RT}}{I} \times 100\,\%$$

where $Q_i$ is the electrons transferred into product $x$ and $Q_{total}$ stands for the total charge consumption. Specifically, $n$ is the number of transferred electrons (2 for CO, 8 for methane, 12 for ethylene), $m$ is the flux of outlet gas products, $v$ is the volume fraction of product determined by gas chromatography, $F$ is the Faradaic constant (96485 C $mol^{-1}$), $p$ is the gas pressure, $T$ is the room temperature and $R$ is the ideal gas constant with a value of 8.314 J $mol\ K^{-1}$, and $I$ is the recorded total current. The overall cell energy efficiency (EE) is calculated by following equation, based on the thermoneutral potential of each product [2].

$$EE = \sum \frac{E^n_{(x)}}{E_{cell}} \times FE_{(x)}$$

$$E^n_{(x)} = \frac{\Delta H_{(x)}}{nF}$$

For example, the enthalpy change ($\Delta H$) of the overall reaction of $CO_2 + 2H_2O \rightarrow CH_4 + 2O_2$ is 890 kJ $mol^{-1}$, which gives a thermoneutral potential $E^n$ of 1.15 V. The calculation methods are given in Supplementary Information.

## 3. Results and discussion

### 3.1. Characterization of electrodes

Fig. 2a presents an SEM image of the commercial copper catalyst used, highlighting discernible nanoparticles despite some inevitable agglomeration. The crystal structure and phase purity of the catalyst were analyzed using XRD (Fig. 2b). The characteristic peaks at 43.1°, 50.4°, and 74.2° correspond to the (111), (200), and (220) planes of copper, respectively, as indexed by JCPDS No. 04–0836. Additionally, two minor peaks attributed to CuO, identified by JCPDS No. 48–1548, indicate partial oxidation of the copper. Diffraction peaks corresponding to the (111), (200), (220), and (311) planes of silver, as indexed by JCPDS No. 65–2871, are also observed in both types of tandem electrodes [25–27]. The cross-sectional SEM image (Fig. 2c) shows that the sprayed copper catalyst layer presents a uniform thickness of about 5 μm on the carbon GDL, and the top view in Fig. S1 also shows that the catalyst uniformly covers the GDL. The prepared Cu@C electrode exhibits superhydrophobicity over 149°, as shown in Fig. S2, which is expected to accelerate the gas transport in the three-phase interface reaction during the catalytic process [28]. In addition, Fig. 2d provides a cross-sectional view of the CuAg electrode after the deposition of two catalyst layers, while Fig. S3 shows that of the AgCu electrode,

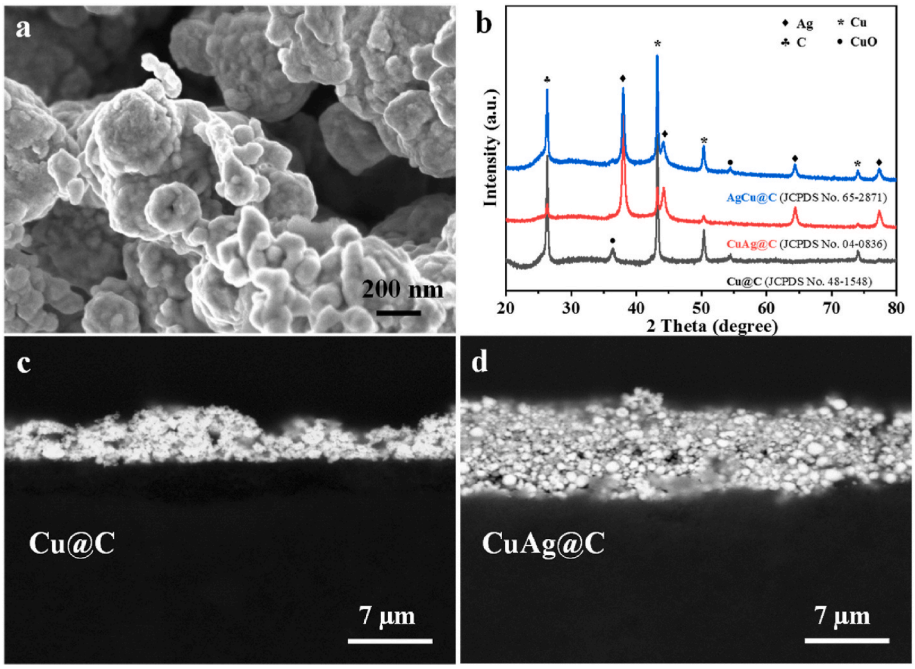


**Fig. 2.** (a) SEM image of commercial copper nanoparticles. (b) XRD patterns of the Cu electrode, tandem CuAg@C, and AgCu@C electrodes. Cross-sectional SEM images of air-sprayed (c) Cu and (d) CuAg catalyst layers on the carbon GDL.

demonstrating a seamless and continuous coating without visible boundaries or cracks. The total catalyst layer thickness measures approximately 8 μm, reflecting the uniformity of the deposition process across the electrode surface. These structural and morphological findings confirm the successful fabrication and integration of the catalyst layers.

### 3.2. Effect of temperature on $CO_2RR$ in alkaline electrolyte

Although electrolyzers are subject to varying external environments in practical applications, temperature is an underrated parameter when evaluating a $CO_2RR$ system [29]. Therefore, the distribution of products and the energy conversion over copper catalysts in the zero-gap electrolyzer with 1 M KOH anolyte was systematically investigated here from room temperature to a maximum of 80 °C. At room temperature, a total current of 1.2 A (current density of 100 mA/cm$^2$), was achieved at a cell voltage of 2.62 V, while a higher current of 2.4 A (current density of 200 mA/cm$^2$) corresponded to a cell voltage of 3.04 V, as shown in Fig. 3a. At a current density of 100 mA/cm$^2$, the Faradaic efficiency (FE) for CO, $C_2H_4$, and $C_3$ products was 6.25 %, 7.82 %, and 4.28 %, respectively. When the current density increased to 200 mA/cm$^2$, the FE for CO dropped to 3.58 %, the one for $C_2H_4$ increased slightly to 8.79 %, and $C_3$ products experienced a sharp decline to 1.81 % FE (Fig. 3b). These findings highlight that at ambient temperature, the alkaline system achieves moderate selectivity for ethylene even at high current densities. At the same time, $C_3$ compound formation is constrained due to the competition from HER and other $C_2$ products.

Raising the reaction temperature to 50 °C substantially reduced energy requirements, as a current density of 100 mA/cm$^2$ was achieved at 2.45 V, while 200 mA/cm$^2$ was obtained at 2.91 V. As illustrated in Fig. 3c, the FE for CO at 100 mA/cm$^2$ rises markedly to 23.14 %, while the FEs for $C_2H_4$ and $C_3$ products reached 9.50 % and 5.29 %, respectively. At 200 mA/cm$^2$, CO selectivity dropped to 9.31 %, whereas $C_2H_4$ formation increased to 11.82 %, and $C_3$ products decreased to 1.10 %. The higher temperature likely enhances CO desorption kinetics and reaction rates, leading to increased CO production at moderate current densities. Furthermore, the acceleration of carbon-carbon coupling kinetics can contribute to the increased generation of $C_2$ products, albeit at the cost of diminished $C_3$ selectivity at higher current densities. When the temperature was elevated to 80 °C, the system achieved further reductions in voltage demands, reaching 100 mA/cm$^2$ at 2.3 V and 200 mA/cm$^2$ at 2.71 V. The Nyquist plots in Fig. S4 clearly show that increasing temperature increases ionic conductivity, reduces cell impedance, and thus improves power conversion. However, the product distribution undergoes significant changes at this elevated temperature. As Fig. 3d reveals, CO exhibited an FE of 14.46 % at the current density

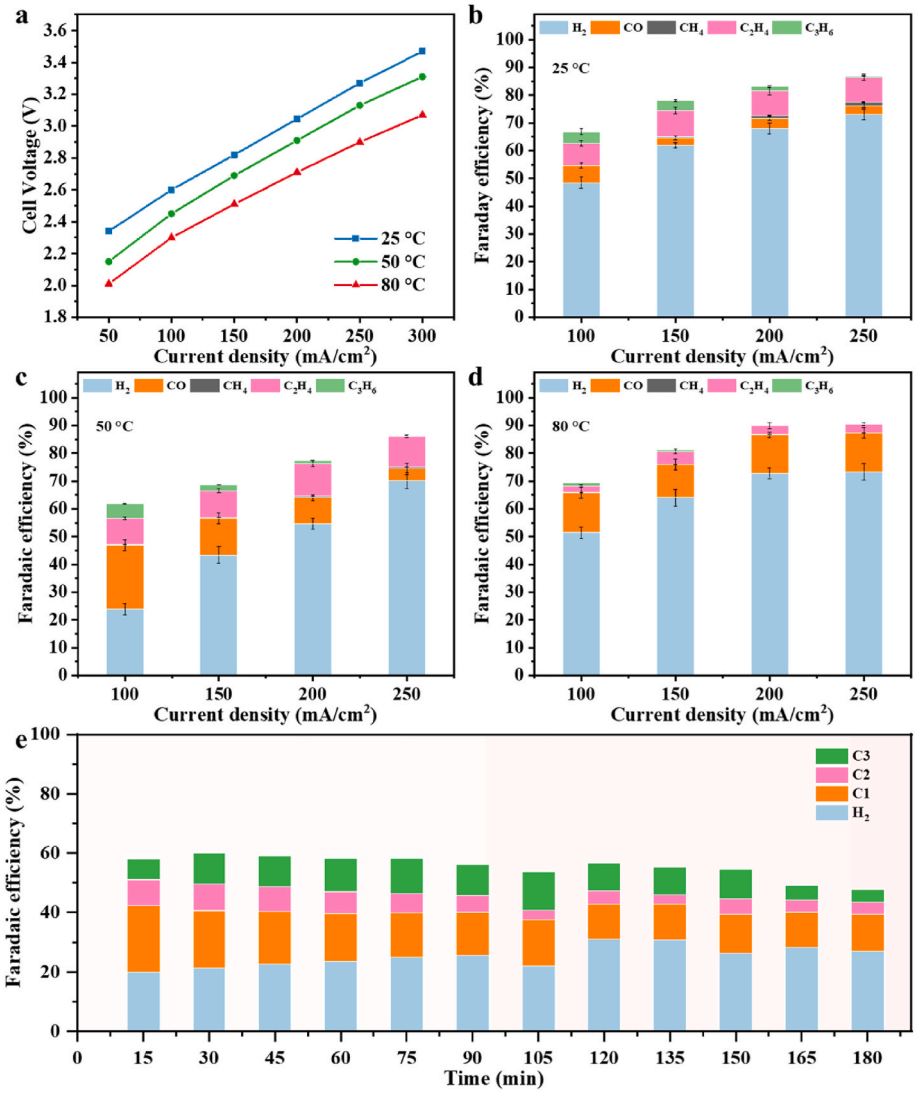


**Fig. 3.** Electrocatalytic $CO_2RR$ performance in 1 M KOH anolyte. (a) Polarization curves at several operating temperatures. Faradaic efficiencies of the products at reaction temperatures of (b) 25 °C, (c) 50 °C, and (d) 80 °C. (e) Stability of the electrolytic reaction at 1.2 A at 50 °C.

of 100 mA/cm$^2$, while the FEs for $C_2H_4$ and $C_3$ products declined to 2.33 % and 1.10 %, respectively. At 200 mA/cm$^2$, CO remained a high FE of 13.90 %, but $C_2H_4$ FE was restricted to 3.10 %. These shifts suggest that higher temperatures favor CO formation but destabilize the intermediates required for the synthesis of $C_2$ and $C_3$ products. Additionally, the increased activity of HER at elevated temperatures likely suppresses the formation of higher hydrocarbons by enhancing proton availability. The energy efficiency of $CO_2$RR depends on the reaction selectivity and overpotential, which is calculated and shown in Fig. S5. At a reaction temperature of 50 °C, the energy efficiency at a current density of 100 mA/cm$^2$ exceeds 20 %, which is attributed to the increased Faradaic efficiency of the gaseous products and the reduced electrolyzer voltage compared to room temperature. At a higher reaction temperature of 80 °C, the energy efficiency does not continue to rise despite the further reduction of the electrolyzer voltage, mainly due to the lower Faradaic efficiency of the desired products, making the energy efficiency 2 %–5 % higher than that at ambient temperature. Although increasing the reaction temperature can reduce the overpotential, this benefit may be offset by the selectivity of the desired products due to the enhancement of side reactions. The stability of the $CO_2$RR process was evaluated over a 3-h operation period at a working current density of 100 mA/cm$^2$ and a reaction temperature of 50 °C, and a GC spectrum for gas content analysis is shown in Fig. S6. While the overall FE for gas-phase products remained relatively stable within the 50 %–60 % range, subtle fluctuations were observed in the selectivity of individual products, as depicted in Fig. 3e. These variations can be attributed to transient shifts in local pH and $CO_2$ coverage near the electrode surface [30]. Despite these variations, the system demonstrated robust stability, maintaining a commendable overall FE for gas-phase products.

Temperature variations exert a profound influence on the interplay between energy efficiency and product selectivity in $CO_2$RR, by directly affecting thermodynamic equilibrium potential and ionic conductivity. Moderate temperatures around 50 °C strike an optimal balance by reducing energy demands while enhancing the production of CO and $C_2H_4$. However, at higher temperatures, while energy efficiency is further improved, the selectivity for complex products like $C_2H_4$ and $C_3$ diminishes. These findings underscore the necessity of optimizing operational parameters to achieve desired product outcomes. Moreover, monitoring both overall efficiency and product distribution during extended operation at a given current is crucial for exploring the interaction between reaction conditions and catalyst performance, thereby supporting the development of robust $CO_2$RR systems.

### 3.3. *Effect of pressure on $CO_2$RR in alkaline electrolyte*

The solubility of $CO_2$ can be increased in the pressurized H-cell, which increases the local $CO_2$ coverage of the catalyst surface and thus improves the productivity of liquid products [31–33]. However, the collection and analysis of products in high-pressure zero-gap electrolyzers is still less discussed, which puts more stringent requirements on catalyst stability and reactor design [34,35]. Here, the influence of high-pressure conditions exceeding 10 bar on the performance of $CO_2$RR in a 1 M KOH electrolyte was systematically evaluated in the modifier electrolyzer. At a current density of 100 mA/cm$^2$, the cell voltage was 2.49 V at an operating pressure of 10 bar, while it decreased to 2.44 V at 15 bar and further to 2.42 V at 20 bar. When the current density increased to 200 mA/cm$^2$, the cell voltage raised to 2.98 V at 10 bar, 2.94 V at 15 bar, and 2.87 V at 20 bar. This trend persisted at a current density of 300 mA/cm$^2$, with cell voltages recorded at 3.45 V, 3.33 V, and 3.28 V for operation pressures of 10 bar, 15 bar, and 20 bar, respectively (Fig. 4a). The increase in pressure slightly reduced the activation barriers for these reactions as shown in Pourbaix diagram (Fig. S7) derived from the Nernst equation [21], which is consistent with the slight decrease in cell voltage observed in the polarization curves at high pressure, indicating that high pressure is thermodynamically beneficial for $CO_2$RR.

The Faradaic efficiencies for various products reveal considerable variations in selectivity for hydrogen and carbon-based products across different pressures. At 10 bar, the CO FE was 24.92 % at 100 mA/cm$^2$ but decreased to 8.98 % at 200 mA/cm$^2$ and further to 3.83 % at 300

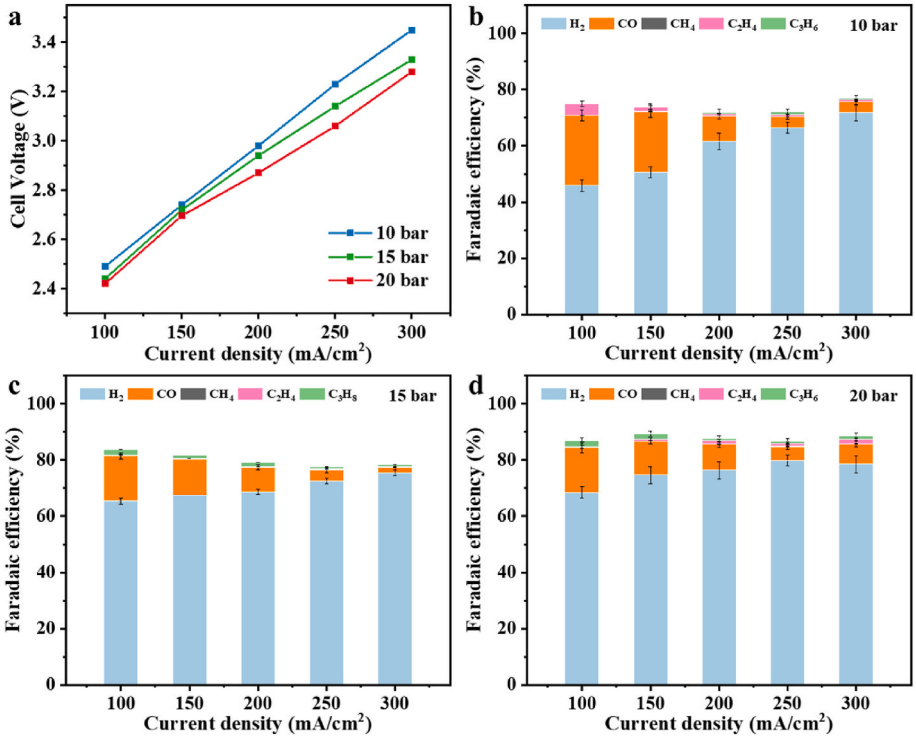


**Fig. 4.** Electrocatalytic performance under high-pressure conditions in 1 M KOH anolyte. (a) Polarization curves. Faradaic efficiencies of the products at a reaction pressure of (b) 10 bar, (c) 15 bar, and (d) 20 bar.

mA/cm$^2$. Ethylene exhibited an FE of 4.02 % at 100 mA/cm$^2$ but became negligible at higher current densities, reaching only 0.86 % FE at 200 mA/cm$^2$ and 0.78 % at 300 mA/cm$^2$ (Fig. 4b). In contrast, hydrogen production showed a clear increase, with FEs of 45.87 %, 61.56 %, and 71.79 % at current densities of 100, 200, and 300 mA/cm$^2$, respectively. At 15 bar, the product distribution shifted significantly (Fig. 4c). At a current density of 100 mA/cm$^2$, the CO FE decreased to 16.08 %, while ethylene became negligible, and $C_3$ compound production rose slightly to 1.88 % FE. As the current density increased, the CO FE dropped further to 8.73 % at 200 mA/cm$^2$ and 1.87 % at 300 mA/cm$^2$. Ethylene FE remained minimal across all current densities, while $C_3$ product FE exhibited a slight increase at both 100 and 300 mA/cm$^2$. Hydrogen production continued to dominate, with an FE of 75.55 % at 300 mA/cm$^2$, reflecting the fierce competition between hydrogen evolution and $CO_2$ reduction. A similar trend is observed at 20 bar (Fig. 4d). At 100 mA/cm$^2$, the CO FE remained at 16.08 %, accompanied by a modest increase in ethylene production (0.26 %) and a higher $C_3$ FE (2.13 %). At 200 mA/cm$^2$, the CO FE declined to 9.25 %, while ethylene and $C_3$ FEs were recorded at 1.20 % and 0.82 %, respectively. At 300 mA/cm$^2$, the CO FE further decreased to 7.18 %, with ethylene and $C_3$ FEs slightly increasing to 1.74 % and 1.13 %, respectively. Hydrogen production reached its peak, with an FE of 78.53 % at 300 mA/cm$^2$, again emphasizing the dominance of hydrogen evolution at elevated pressures. Despite the thermodynamic benefits brought by high pressure, $CO_2$RR involving multi-proton coupled electron transfer is also subject to complex kinetics. The formation of $C_2$ and $C_3$ products usually involves multi-step reactions, requiring specific stabilization of intermediates [36]. High pressure can enhance the coverage of $CO_2$ on the catalyst surface, which may block the active sites or change the reaction pathway, such as promoting the desorption of CO instead of allowing it to be firmly attached to the catalyst surface as an intermediate to provide the necessary C–C bonds for high-carbon products. In addition, the transport of water from cathode to anode through the membrane driven by the electric field and concentration gradient [37,38], may further enhance the competitiveness of the hydrogen evolution reaction (HER), especially at higher current densities. Together, these factors lead to the unexpected suppression of $C_2$ and $C_3$ product formation under high-pressure conditions.

The high-pressure experiments revealed a progressive shift towards hydrogen production, with a concurrent decline in selectivity for CO and $C_2$ products. This also underscores the potential of utilizing high-pressure conditions to generate synthesis gas [39], a carbon monoxide and hydrogen mixture, ideal for downstream catalytic applications such as Fischer-Tropsch synthesis which needs a hydrogen to CO molar ratio of approximately 2:1. Thus, the capacity to adjust product selectivity under elevated pressure presents an opportunity for optimizing the integration of $CO_2$RR with subsequent thermal catalytic processes, thereby enabling the efficient synthesis of valuable hydrocarbon fuels.

### 3.4. *Effect of neutral electrolyte on $CO_2$RR performance*

Neutral $KHCO_3$ electrolytes, known for their environmental friendliness, non-toxicity, and wide availability, have emerged as the preferred medium for the $CO_2$ electroreduction reaction, as they can serve as a pH buffer and proton donor [40,41]. Exploring the concentration-dependent effects of a $KHCO_3$ anolyte within the zero-gap electrolyzer provides fundamental insight into the underlying reaction mechanisms.

As illustrated in Fig. 5a and Fig. 5b for a 0.1 M $KHCO_3$ anolyte system, the cell voltage stabilized at approximately 3.43 V under a current density of 100 mA/cm$^2$ (corresponding to a total current of 1.2 A), yielding predominantly gaseous products with the Faradaic efficiencies of ethylene and CO being 15.1 % and 25.4 %, respectively. When the current density increased to 200 mA/cm$^2$, the cell voltage rose to 3.96 V, accompanied by a decline in the FEs for ethylene and CO to 10.1 % and 12.1 %, respectively. The promotion of ethylene formation can be attributed to the facilitation of the CO dimerization pathway. These findings are in agreement with the observations of Peter Strasser et al., who demonstrated that a rapid increase in local pH during electrolysis with low bicarbonate concentrations promotes the formation of $C_2$

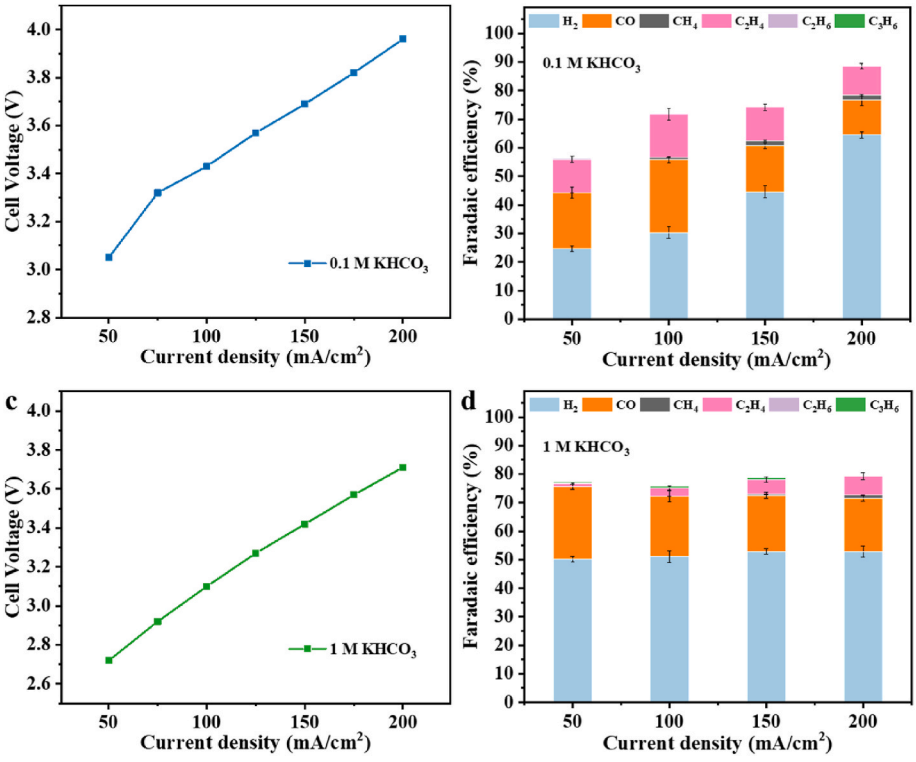


**Fig. 5.** (a) Polarization curves and (b) Faradaic efficiencies of the products in 0.1 M $KHCO_3$ anolyte. (c) Polarization curves and (d) Faradaic efficiencies of the products in 1 M $KHCO_3$ anolyte.

products through C–C coupling [42]. However, the elevated cell voltage reflects the limited ionic conductivity and buffering capacity inherent to dilute electrolytes. The diminished selectivity for carbon-based products at higher potentials arises from intensified competition between proton and electron transfer steps, favoring the HER over the $CO_2$RR. Consequently, the generation of higher hydrocarbons becomes less efficient at elevated current densities in low-concentrated $KHCO_3$ solutions. In contrast, increasing the $KHCO_3$ concentration to 1.0 M significantly lowered the cell voltage to 3.1 V at 100 mA/cm$^2$ and to 3.71 V at 200 mA/cm$^2$ (Fig. 5c). Enhanced ionic conductivity and buffering capacity mitigate ohmic losses, as verified by the Nyquist plots shown in Fig. S8, and stabilize the local pH to facilitate a more energy-efficient reaction. Nevertheless, the FE for CO decreased to 21.2 %, while hydrogen emerged as the dominant product with an FE exceeding 51 % at a current density of 100 mA/cm$^2$, as depicted in Fig. 5d. At a current density of 200 mA/cm$^2$, the predominance of HER became even more pronounced, with hydrogen achieving an FE of 52.9 % and CO further declining to 18.7 %. These trends are consistent with the findings of Kastlunger et al., who reported that higher bicarbonate concentrations favor the production of methane and oxygenated $C_{2+}$ products, often at the expense of ethylene [43]. Although the low-concentration neutral electrolyte system requires a higher voltage, its superior selectivity for $C_1$–$C_3$ products results in a higher energy efficiency (17 %) at a current density of 100 mA/cm$^2$ than that of the high-concentration anodic electrolyte system, as shown in Fig. S9.

The concentration of the neutral electrolyte exerts a profound influence on ethylene production, necessitating a delicate balance between energy efficiency, product selectivity, and operational stability. While higher $KHCO_3$ concentrations improve ionic conductivity and reduce cell voltage, the product distribution shifts toward HER, thereby limiting $C_{2+}$ product yield. Conversely, lower concentrations favor the selectivity for ethylene but at the cost of increased energy requirements. Thus, the interplay between electrolyte concentration and reaction rate emerges as a critical factor in regulating product distribution during neutral $CO_2$RR.

### 3.5. Effect of tandem catalysts on $CO_2$RR

Tandem catalyst layer electrodes integrate silver with its high CO selectivity and copper capable of generating $C_{2+}$ products to facilitate and establish a cascade reaction system [44,45]. Owing to the dual functionality, this system divides the $CO_2$ reduction reaction into two steps: $CO_2$-to-CO and CO-to-$C_2$ at different catalytic sites, increasing surface *CO coverage and enhancing C–C coupling [46]. Here, an AgCu tandem catalyst electrode was prepared by spraying a silver catalyst layer on the GDL first, followed by a copper catalyst layer, and the reverse order was identified with CuAg. EDS mapping of the two hybrid electrodes demonstrates the uniform distribution of elements and the dominance of the upper metal elements, as shown in Figs. S10 and S11. While the migration or mixing of metal catalyst particles may potentially occur, no obvious evidence was detected in the XRD and SEM images. Therefore, it is assumed that such phenomena will not have a decisive impact on the experimental results.

In an alkaline electrolyte, the AgCu electrode still demonstrated a low voltage demand, achieving 2.7 V at 100 mA/cm$^2$ and 3.08 V at 200 mA/cm$^2$, as Fig. 6a illustrated. The Faradaic efficiency at 100 mA/cm$^2$ was 24.14 % for CO, while ethylene and hydrogen showed 2.07 % and 55.08 %, respectively. When the current density increased to 200 mA/cm$^2$, the CO FE declined significantly to 12.21 %, accompanied by a minor increase in $C_2H_4$ FE to 2.26 % and a notable rise in $H_2$ FE to 66.75 %, as shown in Fig. 6b. The CuAg electrode required slightly lower voltages of 2.6 V at 100 mA/cm$^2$ and a higher one of 3.14 V at 200 mA/cm$^2$. The CO FE was initially lower at 20.63 %, with no detectable ethylene production at 100 mA/cm$^2$. However, $H_2$ dominated the product distribution with an FE of 71.15 %. At 200 mA/cm$^2$, the CO FE further decreased to 13.07 %, while $C_2H_4$ appeared with an FE of 1.16 %, and $H_2$ increased to 74.90 % in Fig. 6c. In neutral electrolytes, the AgCu electrode required a cell voltage of 2.91 V at 100 mA/cm$^2$ and

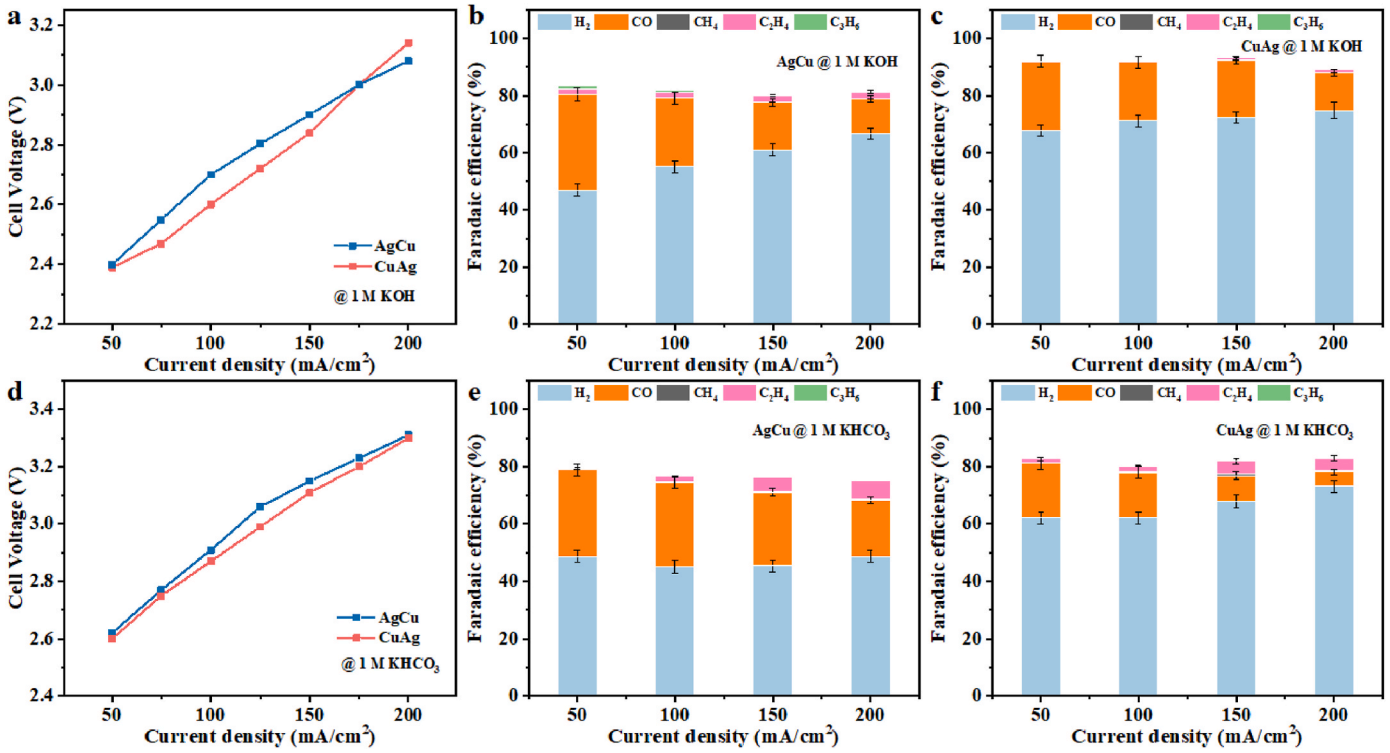


**Fig. 6.** (a) Polarization curves of two types of Ag/Cu tandem catalysts in 1 M KOH anolyte. Faradaic efficiencies of the products from (b) AgCu and (c) CuAg catalysts in an alkaline system. (d) Polarization curves of the tandem electrodes in 1 M $KHCO_3$ anolyte. Faradaic efficiencies of the products from (e) AgCu and (f) CuAg electrodes in a neutral system.

3.31 V at 200 mA/cm$^2$ (Fig. 6d), producing CO with an FE of 29.44 % at 100 mA/cm$^2$, alongside 1.81 % for $C_2H_4$ and 45.15 % for H2. As the current density rose to 200 mA/cm$^2$, the CO FE declined to 19.71 %, but the $C_2H_4$ FE increased significantly to 6.50 %, as depicted in Fig. 6e. For the CuAg electrode, the voltage demands were 2.87 V at 100 mA/cm$^2$ and 3.3 V at 200 mA/cm$^2$. At 100 mA/cm$^2$, the CO FE was 15.80 %, with $C_2H_4$ and $H_2$ achieving FEs of 2.20 % and 62.14 %, respectively. As shown in Fig. 6f, increasing the current density to 200 mA/cm$^2$ resulted in a drastic drop in CO FE to 4.92 %, a rise in $C_2H_4$ FE to 4.33 %, and an increase in $H_2$ FE to 73.20 %.

The tandem electrode configuration significantly improved CO production and Faradaic efficiency, but the yield of $C_2$–$C_3$ products was still limited compared to Cu electrodes. In addition, the overall improvement in $C_2H_4$ production over Cu-based catalysts in neutral electrolytes compared to alkaline electrolytes suggests that electrolyte composition significantly affects the catalytic pathways. This emphasizes the importance of catalyst design for controlling product selectivity and highlights the critical interplay of optimizing catalyst material properties and electrolyte conditions toward the desired product distribution [47].

## 4. Conclusion

This study systematically explores the effects of key operational factors, including electrolyte concentration, reaction temperature, operating pressure, and catalyst design for $CO_2$RR in a zero-gap electrolyzer. The results demonstrate that electrolyte concentration significantly influences current efficiency and product distribution. Lower concentrations promote the formation of $C_2$ products, while higher concentrations reduce cell voltage and enhance proton transfer but increase competition from the hydrogen evolution reaction. Elevated temperatures improve the reaction kinetics, with moderate temperatures balancing energy consumption and product selectivity, whereas high temperatures suppress higher hydrocarbon formation despite lowering voltage demands. Increased pressure improves local $CO_2$ concentration, reduces cell voltage, and enhances both mass transport and reaction rates, but also intensifies HER competition, diminishing the selectivity for higher hydrocarbons. Furthermore, competition between tandem catalysts enhances CO production, possibly due to differences in intermediate adsorption energies, highlighting the need for precise control in future catalyst design. Overall, the study provides fundamental insights and practical strategies for improving $CO_2$RR system efficiency and product selectivity.

## CRediT authorship contribution statement

**Siyu Zhong:** Writing – original draft, Validation, Methodology, Investigation, Data curation. **Wenwu Yang:** Methodology. **Sida Liu:** Methodology. **Roland Dittmeyer:** Writing – review & editing, Supervision, Funding acquisition.

## Declaration of competing interest

The authors declare that they have no known competing financial interests or personal relationships that could have appeared to influence the work reported in this paper.

## Acknowledgments

We appreciate the financial backing provided by the Helmholtz Association of German Research Centers under the Helmholtz-Program: MTET Materials and Technologies for the Energy Transition (Topic 3: Chemical Energy Carriers), as well as HI-CAM II, Cluster I, Net Zero 2050. S. Zhong thanks Dr. Peter G. Weidler for XRD measurements and Ms. Mengtian Zhuang for assistance in electrode fabrication.

## Appendix A. Supplementary data

Supplementary data to this article can be found online at https://doi.org/10.1016/j.ijhydene.2025.03.234.

## References

[1] Wang P, Yang H, Tang C, Wu Y, Zheng Y, Cheng T, Davey K, Huang X, Qiao SZ. Boosting electrocatalytic $CO_2$-to-ethanol production via asymmetric C-C coupling. Nat Commun 2022;13:3754.
[2] She X, Zhai L, Wang Y, Xiong P, Li MMJ, Wu TS, Wong MC, Guo X, Xu Z, Li H, Xu H, Zhu Y, Tsang SCE, Lau SP. Pure-water-fed, electrocatalytic $CO_2$ reduction to ethylene beyond 1,000 h stability at 10 A. Nat Energy 2024;9:81–91.
[3] Ye Q, Zhao X, Jin R, Dong F, Xie H, Deng B. Advances and challenges in membrane electrode assembly electrolyzers for $CO_2$ reduction. J Mater Chem A 2023;11:21498–515.
[4] Segets D, Andronescu C, Apfel UP. Accelerating $CO_2$ electrochemical conversion towards industrial implementation. Nat Commun 2023;14:7950.
[5] Sun JW, Fu HQ, Liu PF, Chen A, Liu P, Yang HG, Zhao H. Advances and challenges in scalable carbon dioxide electrolysis. EES Catalysis 2023;1:934–49.
[6] Tian H, Zhang ZY, Fang H, Jiao H, Gao TT, Yang JT, Bian L, Wang ZL. Selective electrooxidation of methane to formic acid by atomically dispersed $CuO_x$ and its induced Lewis acid sites on $V_2O_5$ in a tubular electrode. Appl Catal, B: Environ Energy 2024;351:124001.
[7] Li L, Li X, Sun Y, Xie Y. Rational design of electrocatalytic carbon dioxide reduction for a zero-carbon network. Chem Soc Rev 2022;51:1234–52.
[8] Yan T, Chen X, Kumari L, Lin J, Li M, Fan Q, Chi H, Meyer TJ, Zhang S, Ma X. Multiscale $CO_2$ electrocatalysis to $C_{2+}$ products: reaction mechanisms, catalyst design, and device fabrication. Chem Rev 2023;123:10530–83.
[9] El-Nagar GA, Haun F, Gupta S, Stojkovikj S, Mayer MT. Unintended cation crossover influences $CO_2$ reduction selectivity in Cu-based zero-gap electrolysers. Nat Commun 2023;14:2062.
[10] Gao DF, Arán-Ais RM, Jeon HS, Roldan Cuenya B. Rational catalyst and electrolyte design for $CO_2$ electroreduction towards multicarbon products. Nat Catal 2019;2:198–210.
[11] Li J, Kuang Y, Zhang X, Hung WH, Chiang CY, Zhu G, Chen G, Wang F, Liang P, Dai H. Electrochemical acetate production from high-pressure gaseous and liquid $CO_2$. Nat Catal 2023;6:1151–63.
[12] Kim JYT, Sellers C, Hao S, Senftle TP, Wang H. Different distributions of multi-carbon products in $CO_2$ and CO electroreduction under practical reaction conditions. Nat Catal 2023;6:1115–24.
[13] Qi K, Zhang Y, Onofrio N, Petit E, Cui X, Ma J, Fan J, Wu H, Wang W, Li J, Liu J, Zhang Y, Wang Y, Jia G, Wu J, Lajaunie L, Salameh C, Voiry D. Unlocking direct $CO_2$ electrolysis to $C_3$ products via electrolyte supersaturation. Nat Catal 2023;6:319–31.
[14] Shin H, Hansen KU, Jiao F. Techno-economic assessment of low-temperature carbon dioxide electrolysis. Nat Sustain 2021;4:911–9.
[15] Ozden A, De Arquer FPG, Huang JE, Wicks J, Sisler J, Miao RK, O'Brien CP, Lee G, Wang X, Ip AH, Sargent EH, Sinton D. Carbon-efficient carbon dioxide electrolysers. Nat Sustain 2022;5:563–73.
[16] Gawel A, Jaster T, Siegmund D, Holzmann J, Lohmann H, Klemm E, Apfel UP. Electrochemical $CO_2$ reduction - the macroscopic world of electrode design, reactor concepts & economic aspects. iScience 2022;25:104011.
[17] Niu ZZ, Gao FY, Zhang XL, Yang PP, Liu R, Chi LP, Wu ZZ, Qin S, Yu X, Gao MR. Hierarchical copper with inherent hydrophobicity mitigates electrode flooding for high-rate $CO_2$ electroreduction to multicarbon products. J Am Chem Soc 2021;143:8011–21.
[18] Wang M, Lin L, Zheng Z, Jiao Z, Hua W, Wang G, Ke X, Lian Y, Lyu F, Zhong J, Deng Z, Peng Y. Hydrophobized electrospun nanofibers of hierarchical porosity as the integral gas diffusion electrode for full-pH $CO_2$ electroreduction in membrane electrode assemblies. Energy Environ Sci 2023;16:4423–31.
[19] Brückner S, Feng Q, Ju W, Galliani D, Testolin A, Klingenhof M, Ott S, Strasser P. Design and diagnosis of high-performance $CO_2$-to-CO electrolyzer cells. Nat Chem. Eng. 2024;1:229–39.
[20] Sassenburg M, Kelly M, Subramanian S, Smith WA, Burdyny T. Zero-gap electrochemical $CO_2$ reduction cells: challenges and operational strategies for prevention of salt precipitation. ACS Energy Lett 2023;8:321–31.
[21] Kani NC, Olusegun S, Chauhan R, Gauthier JA, Singh MR. High-pressure electrochemistry: a new frontier in decarbonization. EES Catalysis 2024;2:507–21.
[22] Endrődi B, Kecsenovity E, Samu A, Halmágyi T, Rojas-Carbonell S, Wang L, Yan Y, Janáky C. High carbonate ion conductance of a robust PiperION membrane allows industrial current density and conversion in a zero-gap carbon dioxide electrolyzer cell. Energy Environ Sci 2020;13:4098–105.
[23] Endrodi B, Kecsenovity E, Samu A, Darvas F, Jones RV, Torok V, Danyi A, Janaky C. Multilayer electrolyzer stack converts carbon dioxide to gas products at high pressure with high efficiency. ACS Energy Lett 2019;4:1770–7.
[24] Zhong S, Sui P, Holtappels P, Navarrete A, Li F, Dittmeyer R. Robust and efficient electroreduction of $CO_2$ to CO in a modified zero-gap electrochemical cell. Chem Eng J 2025;509:161119.
[25] Mardiansyah D, Badloe T, Triyana K, Mehmood MQ, Raeis-Hosseini N, Lee Y, Sabarman H, Kim K, Rho J. Effect of temperature on the oxidation of Cu nanowires and development of an easy to produce, oxidation-resistant transparent conducting electrode using a PEDOT:PSS coating. Sci Rep 2018;8:10639.

[26] Dasireddy VDBC, Neja SŠ, Blaž L. Correlation between synthesis pH, structure and Cu/MgO/$Al_2O_3$ heterogeneous catalyst activity and selectivity in $CO_2$ hydrogenation to methanol. J CO2 Util 2018;28:189–99.
[27] Han C, Ge L, Chen C, Li Y, Zhao Z, Xiao X, Li Z, Zhang J. Site-selected synthesis of novel Ag@AgCl nanoframes with efficient visible light induced photocatalytic activity. J Mater Chem A 2014;2:12594–600.
[28] Hao Q, Zhong H, Wang J, Liu K, Yan JM, Ren Z, Zhou N, Zhao X, Zhang H, Liu D, Liu X, Chen L, Luo J, Zhang X. Nickel dual-atom sites for electrochemical carbon dioxide reduction. Nat Synthesis 2022;1:719–28.
[29] Vos RE, Kolmeijer KE, Jacobs TS, van der Stam W, Weckhuysen BM, Koper MTM. How temperature affects the selectivity of the electrochemical $CO_2$ reduction on copper. ACS Catal 2023;13:8080–91.
[30] Hursan D, Janaky C. Operando characterization of continuous flow $CO_2$ electrolyzers: current status and future prospects. Chem Commun 2023;59:1395–414.
[31] Qiu R, Jia J, Peng L, Li R, Yan S, Li J, Zhang J, Sun DT, Lan Z, Xue T, Xu G, Cui L, Lv Z, Li C, Hong Y, Guo Y, Ren B, Yang S, Li J, Han B. Enhanced electroreduction of $CO_2$ to ethanol via enriched intermediates at high $CO_2$ pressures. Green Chem 2023;25:684–91.
[32] Li J, Kuang Y, Meng Y, Tian X, Hung WH, Zhang X, Li A, Xu M, Zhou W, Ku CS, Chiang CY, Zhu G, Guo J, Sun X, Dai H. Electroreduction of $CO_2$ to formate on a copper-based electrocatalyst at high pressures with high energy conversion efficiency. J Am Chem Soc 2020;142:7276–82.
[33] Huang L, Gao G, Yang C, Li XY, Miao RK, Xue Y, Xie K, Ou P, Yavuz CT, Han Y, Magnotti G, Sinton D, Sargent EH, Lu X. Pressure dependence in aqueous-based electrochemical $CO_2$ reduction. Nat Commun 2023;14:2958.
[34] Dufek EJ, Lister TE, Stone SG, McIlwain ME. Operation of a pressurized system for continuous reduction of $CO_2$. J Electrochem Soc 2012;159:F514–7.
[35] Ramdin M, Morrison ART, de Groen M, van Haperen R, de Kler R, van den Broeke LJP, Trusler JPM, de Jong W, Vlugt TJH. High pressure electrochemical reduction of $CO_2$ to formic acid/formate: a comparison between bipolar membranes and cation exchange membranes. Ind Eng Chem Res 2019;58:1834–47.
[36] Birdja YY, Pérez-Gallent E, Figueiredo MC, Göttle AJ, Calle-Vallejo F, Koper MTM. Advances and challenges in understanding the electrocatalytic conversion of carbon dioxide to fuels. Nat Energy 2019;4:732–45.
[37] Chen Y, Ma T, Wang F, Liu Y. Effect of pressure on the gas diffusion electrodes during $CO_2$ reduction reaction. Ind Eng Chem Res 2024;63:15546–53.
[38] Wheeler DG, Mowbray BAW, Reyes A, Habibzadeh F, He JF, Berlinguette CP. Quantification of water transport in a $CO_2$ electrolyzer. Energy Environ Sci 2020;13:5126–34.
[39] Messias S, Sousa MM, Nunes da Ponte M, Rangel CM, Pardal T, Reis Machado AS. Electrochemical production of syngas from $CO_2$ at pressures up to 30 bar in electrolytes containing ionic liquid. React Chem Eng 2019;4:1982–90.
[40] Hu L, Sai X, Liu X, Chen Z, Wang G, Yi X. Influence of environmental conditions on electrocatalytic $CO_2$ reduction. ChemCatChem 2024;16:e202301335.
[41] Li T, Shao M. A minireview on electrochemical $CO_2$ conversion based on carbonate/bicarbonate media. EES Catalysis 2024;2:564–72.
[42] Varela AS, Kroschel M, Reier T, Strasser P. Controlling the selectivity of $CO_2$ electroreduction on copper: the effect of the electrolyte concentration and the importance of the local pH. Catal Today 2016;260:8–13.
[43] Kastlunger G, Heenen HH, Govindarajan N. Combining first-principles kinetics and experimental data to establish guidelines for product selectivity in electrochemical $CO_2$ reduction. ACS Catal 2023;13:5062–72.
[44] Chen C, Li Y, Yu S, Louisia S, Jin J, Li M, Ross MB, Yang P. Cu-Ag tandem catalysts for high-rate $CO_2$ electrolysis toward multicarbons. Joule 2020;4:1688–99.
[45] Jiao H, Wang C, Tian H, Zhang ZY, Zhao Y, Na P, Yamauchi Y, Wang ZL. Strong interaction heterointerface of NiFe oxyhydroxide/cerium oxide for efficient and stable water oxidation. Chem Eng J 2024;498:155063.
[46] Chen Y, Li XY, Chen Z, Ozden A, Huang JE, Ou P, Dong J, Zhang J, Tian C, Lee BH, Wang X, Liu S, Qu Q, Wang S, Xu Y, Miao RK, Zhao Y, Liu Y, Qiu C, Abed J, Liu H, Shin H, Wang D, Li Y, Sinton D, Sargent EH. Efficient multicarbon formation in acidic $CO_2$ reduction via tandem electrocatalysis. Nat Nanotechnol 2024;19:311–8.
[47] Zhang ZY, Tian H, Jiao H, Wang X, Bian L, Liu Y, Khaorapapong N, Yamauchi Y, Wang ZL. $SiO_2$ assisted $Cu^0$–$Cu^+$–$NH_2$ composite interfaces for efficient $CO_2$ electroreduction to $C_{2+}$ products. J Mater Chem A 2024;12:1218–32.